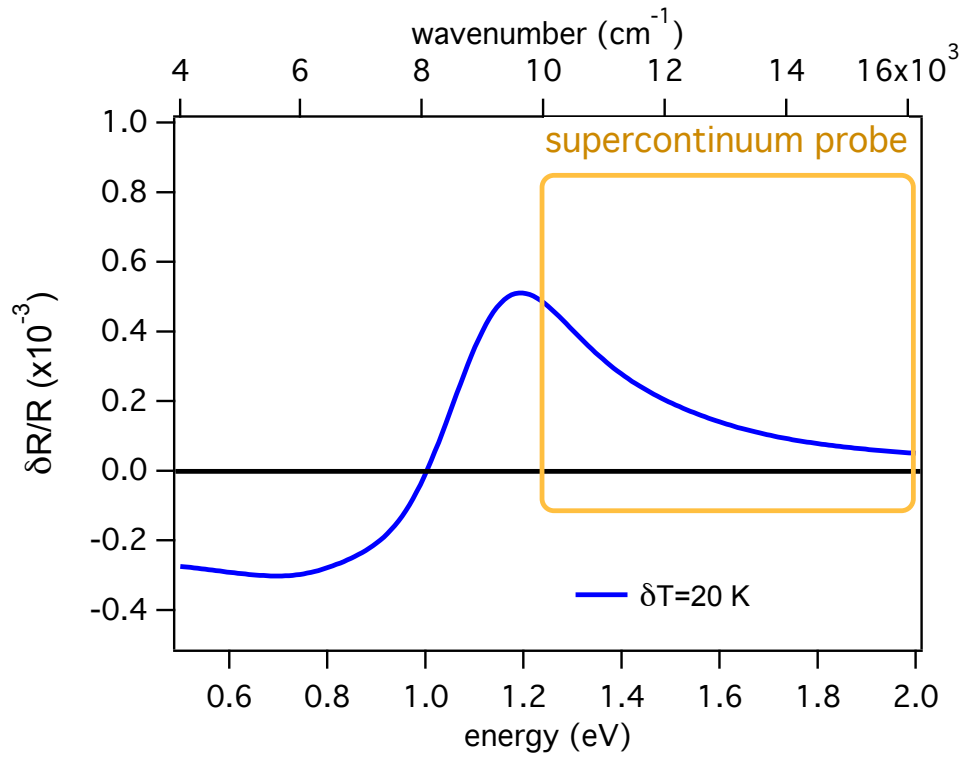


**Supplementary Figure S1. Optical properties of optimally-doped  $\text{Bi}_2\text{Sr}_2\text{Ca}_{0.92}\text{Y}_{0.08}\text{Cu}_2\text{O}_{8+\delta}$ .**

The reflectivity, measured over a broad frequency range by spectroscopic ellipsometry, is reported for OP96 at  $T=300$  K and 100 K. The solid red curves are fits to the data. In the top inset we report  $\epsilon_1$  (right axis) and  $\epsilon_2$  (left axis), measured at  $T=100$  K. The solid lines are the fit to the data. In the bottom inset, the boson spectra  $I^2\chi(\Omega)$ , extracted from the fitting procedure, are reported. All the optical data are reported as a function of the wavenumber ( $\text{cm}^{-1}$ ). The conversion to energy units is  $8064 \text{ cm}^{-1}=1 \text{ eV}$ .



**Supplementary Figure S2. Effective temperature increase.**

The blue solid line is the reflectivity variation calculated for a “quasi-thermal” increase of the temperature  $T$ , i.e.  $\delta T=20$  K.

	parameters	T=20 K	T=100 K	T=300 K
<b>extended Drude</b>	$\epsilon_{\text{inf}}$	2.67	2.67	2.62
	$\omega_p$	17512	17650	16928
	$\Gamma_{\text{imp}}$	53	155	625
<b>mid-infrared peak</b>	$\omega_0$	4234	4929	4264
	$\omega_{p0}^2$	10454991	13871222	22041800
	$\gamma_0$	3535	4706	4069
	$\omega_1$	6490	6959	6789
	$\omega_{p1}^2$	11001998	6489852	8142014
	$\gamma_1$	3519	2949	3925
<b>interband transitions</b>	$\omega_2$	11800	11800	11650
	$\omega_{p2}^2$	5560610	7460610	5307060
	$\gamma_2$	3644	3944	3500
	$\omega_3$	16163	16163	15409
	$\omega_{p3}^2$	40768500	41268500	45542000
	$\gamma_3$	8304	8304	8905
	$\omega_4$	21947	21947	21300
	$\omega_{p4}^2$	225776000	230776025	223159025
	$\gamma_4$	13998	13898	13898
	$\omega_5$	31057	31057	30756
	$\omega_{p5}^2$	288626121	288626121	320536896
	$\gamma_5$	6191	6191	6908
	$\omega_6$	35146	35146	34946
	$\omega_{p6}^2$	217474009	217474009	214474009
	$\gamma_6$	6396	6396	6396
	$\omega_7$	40421	40421	40421
	$\omega_{p7}^2$	750212100	750212100	756371984
	$\gamma_7$	7518	7518	7518

**Supplementary Table S1. Parameters of the equilibrium dielectric function.**

Values of the parameters resulting from the fit to  $\epsilon_1(T, \omega)$  and  $\epsilon_2(T, \omega)$  for OP96. All the values are expressed in inverse centimeter units ( $\text{cm}^{-1}$ ). The values reported in the table are truncated at the last significative figure, considering the standard deviation given by the fitting procedure.

	parameters	t=0.4 ps
extended Drude	T	39
interband transitions	$\omega_2$	11800
	$\omega_{p2}^2$	5679264
	$\gamma_2$	3698
	$\omega_2$	16176
	$\omega_{p2}^2$	40689072
	$\gamma_2$	8283

**Supplementary Table S2. Parameters of the non-equilibrium dielectric function.**

Values of the parameters modified in the differential dielectric function  $\delta\epsilon(\omega,t) = \epsilon_{\text{neq}}(\omega,t) - \epsilon_{\text{eq}}(\omega,t)$  to fit the data at  $T=20$  K for the optimally doped (OD96 sample). The best fit is reported in Fig. 4a of the manuscript.

# Supplementary Note 1

## Equilibrium optical properties of $\text{Bi}_2\text{Sr}_2\text{Ca}_{0.92}\text{Y}_{0.08}\text{Cu}_2\text{O}_{8+\delta}$

In Supplementary Figure S1 we report the reflectivity measured on OP96 by spectroscopic ellipsometry at 300 K and 100 K. The reflectivity measured at 20 K is not reported, since, on the scale of Supplementary Figure S1, it overlaps with the 100 K results. In the top inset to Supplementary Figure S1 we report the real ( $\epsilon_1$ ) and imaginary ( $\epsilon_2$ ) parts of the dielectric function, measured on OP96 at 100 K. From these data we can argue that, below  $10000 \text{ cm}^{-1}$  (1.25 eV),  $\epsilon(\omega)$  is dominated by the Drude response of free carriers coupled to a broad spectrum of bosons [25,26], whereas in the high-energy region ( $\hbar\omega > 1.25 \text{ eV}$ ), a major role is played by the interband transitions. The best fit to the data (solid black lines) is obtained modeling the equilibrium dielectric function as:

$$\epsilon_{\text{eq}}(T, \omega) = \epsilon_D(T, \omega) + \sum_i \epsilon_{L_i}(T, \omega) \quad (\text{S1})$$

where  $\epsilon_D(T, \omega)$  and  $\epsilon_{L_i}(T, \omega)$  represent Drude and Lorentz oscillators, indexed by  $i$ . The reflectivity is obtained from the dielectric function through the relation:

$$R(T, \omega) = \frac{1 - \sqrt{\epsilon(T, \omega)}}{1 + \sqrt{\epsilon(T, \omega)}} \quad (\text{S2})$$

The Drude component of the dielectric function is given by the extended Drude model [25,26]:

$$\epsilon_D(\omega) = -\frac{\omega_p^2}{\omega(\omega + M(\omega, T))} \quad (\text{S3})$$

where  $M(\omega, T)$  is the temperature-dependent memory function, given by:

$$M(\omega, T) = \Gamma_{\text{imp}} - 2i \int_0^\infty d\Omega K(\omega, \Omega; T) I^2 \chi(\Omega) \quad (\text{S4})$$

where  $\Gamma_{\text{imp}}$  is the impurity scattering rate and  $I^2 \chi(\Omega)$  is the spectrum of the bosons coupled to the electrons through the kernel function  $K(\omega, \Omega; T)$ . The kernel function is calculated by [47]:

$$K(x, y) = \frac{i}{y} + \left\{ \frac{y - x}{x} [\Psi(1 - ix + iy) - \Psi(1 + iy)] \right\} - \{y \rightarrow -y\} \quad (\text{S5})$$

where  $x = \omega/2\pi T$  and  $y = \Omega/2\pi T$  and  $\Psi(x, y)$  is the digamma function. In the bottom inset to Supplementary Figure S1 we report the boson spectra  $I^2 \chi(\Omega)$  extracted from the fit at  $T=300 \text{ K}$  and  $T=100 \text{ K}$ . The spectra are characterized by a narrow peak at 50-70 meV and a broad spectrum extending up to 400 meV, in agreement with the literature [25,26]. Below  $T_c$  the far-infrared reflectivity is dominated by the opening of the superconducting gap and by the emergence of the

condensate  $\delta(0)$  function. For this reason, the extraction of the boson spectral function below  $T_c$  is difficult and is still subject of debate [26]. To fit the reflectivity at  $T=20$  K we used the  $I^2\chi(\Omega)$  determined at  $T=100$  K. Neglecting a possible sharp decrease below  $T_c$  of the scattering time [48] does not alter the conclusions of this work.

To satisfactorily reproduce the optical properties both in the underdoped regime, characterized by strong mid-infrared (MIR) peaks, and in the overdoped regime, where the MIR peaks broadens and can be completely accounted for by the extended Drude model, we used a general dielectric function model where both MIR peaks and the  $I^2\chi(\Omega)$  glue are present.

In Supplementary Figure S1, the solid lines are the fit to the data. In Supplementary Table S1 we report all the parameters obtained from the fitting procedure on OP96, at  $T=300$  K,  $T=100$  K and  $T=20$  K.

The best fit to the full spectrum is obtained by including in the fit two oscillators at 0.5 eV and 0.8 eV. The spectral weight of these peaks represents less than 10 percent of the free particle spectral weight and depends strongly on temperature. For this reason this part of the spectrum is part of the high energy range of the generalized Drude peak. Correspondingly, the energy range and intensity of  $I^2\chi(\Omega)$  is higher than shown in the inset of Supplementary Figure S1 [26]. The representation of part of the generalized Drude response by two oscillators at 0.5 eV and 0.8 eV was used for convenience of rapid convergence of the fitting routine, and does not affect the conclusions of this work.

The interband transitions in the near-IR/visible/UV spectral range are reproduced using six Lorentz oscillators at  $\omega_{0i} \sim 1.46, 2, 2.72, 3.85, 4.4$  and  $5$  eV. The number of the interband oscillators has been fixed to the minimum necessary to obtain a stable fit. Adding more oscillators does not significantly improve the  $\chi^2$  of the fit in the 1-5 eV region.

The attribution of the 1.46, 2, 2.72, 3.85 eV transitions, that are the most relevant to this work, is discussed in the manuscript. Interpretation of the 1.46 eV structure in terms of a  $d-d$  excitation [49] can be ruled out, since the oscillator strength obtained from the fit is incompatible with the temperature dependence of a phonon assisted  $d-d$  transition, observed in undoped compounds [50]. The dielectric functions of UD83 and OD86 have been extrapolated from the  $\epsilon_{eq}(T, \omega)$  of OP96, following the trend of the optical properties at different dopings, reported in Ref. 20.

## Supplementary Note 2

### Differential model and non-equilibrium dielectric function

In a time-resolved experiment the impulsive photoinjection of excitations is achieved by an ultrashort laser pulse (FWHM=140 fs) in the near-IR spectral region ( $\lambda=800$  nm). The recovery dynamics of the non-equilibrium (pumped) electronic distribution can be roughly separated in three timescales:

#### i) 0-50 fs electron thermalization

The pump pulse creates a non-thermal population, injecting excitations at  $\sim 1.5$  eV. The scattering rate, obtained through optical measurements, is strongly determined by both electron-electron and electron-phonon scattering processes and is roughly proportional to both the frequency and temperature, i.e.,  $1/\tau(\omega, T) \propto \omega + T$  [51]. At 1.5 eV energy, the frequency-dependent scattering rate is  $\sim 4000$  cm $^{-1}$ , corresponding to lifetime of  $\sim 1$  fs. In the first tens of femtoseconds, the non-equilibrium electrons lose energy through a cascade process and low-energy excitations are accumulated at the top of the gap. As the electronic excitations decrease their energy, the scattering time proportionally decreases. The non-equilibrium population created within the 140 fs pulse duration can be assumed as “quasi-thermal”, being described by an effective chemical potential ( $\mu_{\text{eff}}$ ) and temperature ( $T_{\text{eff}}$ ). In this frame, the photoinduced non-equilibrium population created during the pulse duration (140 fs) is independent of the particular pump photon energy. To test this prediction, we repeated the  $\delta R/R(\omega, t)$  measurements with a photon pump energy of 3.14 eV, obtaining the same results.

The density of photoinjected excitations can be roughly estimated considering the absorbed laser fluence of 10  $\mu\text{J}/\text{cm}^2$  per pulse, corresponding to an absorbed energy density of 0.6 J/cm $^3$ ,  $\lambda_d=160$  nm being the penetration depth at 800 nm wavelength. Considering a volume per Cu atom of  $1.13 \cdot 10^{-22}$  cm $^3$  and assuming that the number of gap-energy excitations produced by each 1.5 eV-photon is approximately  $\sim \hbar\omega/2\Delta_{\text{SC}} = 1.5$  eV/0.04 eV  $\sim 40$ , the density of broken Cooper pairs is  $\sim 5.5 \cdot 10^{-3}$  per Cu atom. This value is about the 7% of the superfluid density in optimally-doped Bi2212 [52]. This calculation does not take into account the d-wave character of the superconducting gap and the possibility that energy can be released to bosons before the complete electron thermalization. A more precise estimation of the density of photoinjected excitation, based on a phenomenological approach, is reported in Supplementary Note 3.

#### ii) 50-500 fs electron and boson thermalization

On this timescale the quasiparticles (QPs) exchange energy with the boson population at the equilibrium temperature  $T_{\text{eq}}$ . The energy exchange can be related either to a direct inelastic scattering process between gap-energy excitations and bosons or to the selective emission of bosons during the recombination of QPs to reform Cooper pairs. On the sub-ps timescale the physical scenario is that of a non-equilibrium population of QPs thermalized with a subset of bosonic modes at a temperature larger than  $T_{\text{eq}}$ .

#### iii) >500 fs boson thermalization

On this timescale the subset of bosons strongly coupled to the QPs thermalizes with the boson thermal reservoir through inelastic boson-boson scattering processes.

This schematic physical picture is confirmed by recent results obtained by different techniques, such as time-resolved photoemission [53], time-resolved electron-diffraction [54] and time-resolved Raman scattering [55].

The reflectivity variations ( $\delta R/R(\omega, t) = R_{\text{neq}}/R_{\text{eq}}(\omega, t) - 1$ ) measured by the TROS technique are related to the variation of the dielectric function  $\delta \epsilon(\omega, t) = \epsilon_{\text{neq}}(\omega, t) - \epsilon_{\text{eq}}(\omega, t)$ . Fitting a differential dielectric function to the measured  $\delta R/R(\omega, t)$ , allows us to obtain the dynamics of  $\epsilon_{\text{neq}}(\omega, t)$ .

In Supplementary Figure S2 (blue line) we report the calculated differential reflectivity, i.e.  $\delta R = R(\omega, T + \delta T)/R(\omega, T) - 1$ , as the effective temperature of the system is changed of  $\delta T = 20$  K. Qualitatively a “quasi-thermal” temperature variation induces a positive change of the reflectivity above 1 eV and a negative variation below 1 eV. Above 1.2 eV the reflectivity variation amplitude monotonically decreases as the photon energy increases. This shape of the reflectivity variation is typical of a temperature-related broadening of the Drude peak. While an effective temperature variation is assumed to satisfactorily fit the data at  $T = 300$  K (see Figure 3), this effect cannot account for the frequency-resolved reflectivity variations measured in both the pseudogap (PG,  $T = 100$  K) and the superconducting (SC,  $T = 20$  K) phases. The signals measured in the PG and SC phases are thus the fingerprint of a genuine modification of the dielectric function as excitations are photo-injected, well beyond a simple broadening of the Drude peak. In the PG, the flat negative signal above  $\sim 1.4$  eV (see Figure 3a,b,c) is well reproduced assuming an impulsive modification of the extended Drude model parameters, such as a weakening of the electron-boson coupling, without invoking any variation of the interband oscillators.

To reproduce the reflectivity variation in the SC phase (see Figure 4a) we must assume a modification of the first two interband oscillator ( $\omega_2$  and  $\omega_3$  in Supplementary Table S1) at  $11800 \text{ cm}^{-1}$  (1.46 eV) and  $16163 \text{ cm}^{-1}$  (2 eV). The conservation of the total spectral weight is guaranteed by the constraint that the sum of the squared plasma frequencies of the extended Drude model and of the interband oscillators is constant. In Supplementary Table S2 we report the parameters modified in  $\epsilon_{\text{neq}}(\omega, t)$  to obtain the best fit to the data, reported in Fig. 4a of the manuscript. The results of the differential fitting procedure are very stable on the choice of the equilibrium dielectric function, obtained in the Supplementary Note 1. The same results are obtained assuming a different  $\epsilon_{\text{eq}}(\omega, t)$  (for example with a different number of interband oscillators or a different glue function). For this reason, the equilibrium dielectric function used can be considered as a “realistic” dielectric function, even if, possibly, not the best dielectric function one can get (since the procedure to obtain it is often questionable). In Figure 4e, the error bars indicate the range of  $\delta \text{SW}_{\text{tot}}$  values that can be obtained starting from different  $\epsilon_{\text{eq}}(\omega, t)$ .

The differential dielectric function fitting procedure allows us to conclude that, as  $T_c$  is crossed, the  $\delta R/R(\omega, t)$  signal measured in the near IR/visible region is associated to a modification of the interband transitions, beyond a simple impulsive broadening of the Drude function. This conclusion holds for all the doping regimes investigated in the present measurements. These results finally shed light on the long-standing question [31,56] about the origin of the  $\delta R/R(t)$  measured in the one-colour time-resolved reflectivity experiment [31,32]. The measured signal is not originated by an *excited state absorption*, related to the variation of the electronic distribution within the unvaried electronic bands, but to a real modification of the underlying electronic excitations and, in particular, of the interband transitions at 1.5-2 eV. Nonetheless, the measured  $\delta R/R(\omega, t)$  is proportional to the density of photo-injected quasiparticles, as commonly assumed (see Ref. [57] and references therein).



## Supplementary Note 3

### Excitation density

In the Supplementary Note 1 we reported an estimation of the total number of excitations impulsively injected in the system by the pump pulse. However, the calculation does not take into account both the d-wave character of the superconducting gap and the possibility that energy can be released to bosons before the complete electron thermalization [21]. A more precise calculation of the density of photoinjected excitations is based on a phenomenological approach. We take advantage of the upper limit in the photoexcitation density set by the photo-induced phase transition to the normal state reported at high pump fluence on HTSC [57,24,58]. This non-thermal phase transition has a first-order character and takes place at a finite superconducting gap value [22], as predicted by the  $\mu_{\text{eff}}$  non-equilibrium superconductivity model [59,21,24].

In the Y-Bi2212 we observe a photo-induced phase transition at  $\sim 60 \mu\text{J}/\text{cm}^2$  [22,24]. From numerical calculations, performed by Nicol et al. [21] within the  $\mu_{\text{eff}}$  model, the instability of the superconducting state is predicted when 15-20% of Cooper pairs are broken. Extrapolating back to our working fluence ( $10 \mu\text{J}/\text{cm}^2$ ), we can estimate the number of photo-excited Cooper pairs to be around 3%.

## Supplementary Note 4

### Gap suppression

When a superconducting system is strongly perturbed by an ultra-short laser pulse, the superconducting order parameter  $\Delta_{SC}$  is expected to exhibit strong variations in time. To obtain the instantaneous gap value during the recovery dynamics we developed a time dependent model based on the Rothwarf-Taylor equations (RTE) [60,22]:

$$\begin{aligned}\dot{n} &= I_{QP}(t) + 2\gamma p - \beta n^2 \\ \dot{p} &= I_{ph}(t) - \gamma p + \beta n^2/2 - \gamma_{esc}(t) \cdot (p - p_T)\end{aligned}\tag{S6}$$

describing the density of excitations  $n$  (quasiparticles, QP) coupled to phonons,  $p$  being the gap-energy phonon density. The non-equilibrium QPs and phonons are photo-injected in the system through the  $I_{QP}(t)$  and  $I_{ph}(t)$  terms. A gaussian temporal profile of  $I_{QP}(t)$  and  $I_{ph}(t)$ , with the same time-width as the laser pulse, is assumed. The coupling of the electronic and phonon population is obtained through: a) the annihilation of a Cooper pair via a gap-energy phonon absorption ( $\gamma p$  term) and b) the emission of gap-energy phonons during the two-body direct recombination of excitations to form a Cooper pair ( $\beta n^2$  term).

In the phonon bottleneck regime ( $\gamma > \gamma_{esc}$ ), the relaxation of the excitations is ultimately regulated by the escape rate of the non-equilibrium gap-energy phonons ( $\gamma_{esc}(p-p_T)$  term,  $p_T$  being the thermal phonon density). The  $\gamma_{esc}$  value is determined both by the escape rate of the non-equilibrium phonons from the probed region and by the energy relaxation through inelastic scattering with the thermal phonons and is directly dependent on the superconducting gap value [22]. The time evolution of  $\Delta_{SC}(t)$  can be obtained from the  $\delta R/R(t)$  time-traces at 800 nm probe wavelength (see Figure 2), under the following assumptions:

- The  $\delta R/R(t)$  time-trace is assumed to be proportional to the solution  $n(t)$  of Eqs. (S6), in agreement with the literature [24,29-33,41,57,61-63].
- the time-dependent non-equilibrium superconducting gap  $\Delta_{SC}(n(t))$  can be expressed as a function of  $n(t)$ , considering the effective temperature ( $T_{eff}$ ) and chemical potential ( $\mu_{eff}$ ) models [59,21,24,22]. In both cases the normalized  $\Delta_{SC}(n(t))$  depends on  $(1-a \cdot n(t)^{3/2})$  (being  $a$  a conversion factor) for a  $d$ -wave gap symmetry [21,22].
- While  $\gamma$  and  $\beta$  can be assumed as constant during the decay dynamics,  $\gamma_{esc}(\Delta_{SC}(n(t)))$  is the only time-dependent parameter.
- $\gamma_{esc}(t)$  quadratically depends on the instantaneous gap value, as demonstrated in Ref. [22], i.e.  $\gamma_{esc}(t) = \gamma_{esc}(0) \cdot [\Delta_{SC}(n(t))/\Delta_{SC}(0)]^2$ ,  $\gamma_{esc}(0)$  being the  $\gamma_{esc}$  value corresponding to the unperturbed gap  $\Delta_{SC}(0)$ .

Fitting the  $\delta R/R(t)$  time-traces (Figure 2), measured at  $10 \mu\text{J}/\text{cm}^2$  pump fluence, with the solution of Eqs. (S6) we are able to extract the instantaneous  $\Delta_{SC}(t)$  value, reported in Figure 4b. The minimum gap value is obtained at  $t=400$  fs delay and corresponds to  $\sim 80\%$  of  $\Delta_{SC}(0)$ .

## Supplementary References

47. Maksimov, E.G. High-temperature superconductivity: the current state. *Physics-Uspekhi* **43**, 965-990 (2000).
48. Marsiglio, F. Sum rule anomaly from suppression of inelastic scattering in the superconducting state. *Phys. Rev. B* **73**, 064507 (2006).
49. Brookes, N.B., *et al.* A determination of the pairing interaction in the high  $T_c$  cuprate superconductor  $\text{Ti}_2\text{Ba}_2\text{CaCu}_2\text{O}_8$  (Ti2212). *Physica C* **460-462**, 40 (2007).
50. Bassi, M., Camagni, P., Rolli, R., Samoggia, G., Parmigiani, F., Dhalenne, G., & Revcolevschi, A. Optical absorption of  $\text{CuGeO}_3$ . *Phys. Rev. B* **54**, R11 030 (1996).
51. van der Marel, D., *et al.* Quantum critical behaviour in a high- $T_C$  superconductor. *Nature* **425**, 271 (2003).
52. Hwang, J., Timusk, T., Gu, G.D.. Doping dependent optical properties of  $\text{Bi}_2\text{Sr}_2\text{CaCu}_2\text{O}_{8+\delta}$ . *J. Phys.: Condens. Matter* **19**, 125208 (2007).
53. Perfetti, L. *et al.* Ultrafast Electron Relaxation in Superconducting  $\text{Bi}_2\text{Sr}_2\text{CaCu}_2\text{O}_{8+\delta}$  by Time-Resolved Photoelectron Spectroscopy. *Phys. Rev. Lett.* **99**, 197001 (2007).
54. Carbone, F., Yang, D.-S, Giannini, E., & Zewail, A.H. Direct role of structural dynamics in electron-lattice coupling of superconducting cuprates. *Proc. Natl. Acad. Sci.* **105**, 20161-20166 (2008).
55. Saichu, R.P. *et al.* Two-Component Dynamics of the Order Parameter of High Temperature  $\text{Bi}_2\text{Sr}_2\text{CaCu}_2\text{O}_{8+\delta}$  Superconductors Revealed by Time-Resolved Raman Scattering. *Phys. Rev. Lett.* **102**, 177004 (2009).
56. Demsar, J., Averitt, R.D., Kabanov, V.V., & Mihailovic D. *et al.* Comment on “Photoinduced Changes of Reflectivity in Single Crystals of  $\text{YBa}_2\text{Cu}_3\text{O}_{6.5}$  (Ortho II)”. *Phys. Rev. Lett.* **91**, 169701 (2003).
57. Kusar, P., *et al.* Controlled Vaporization of the Superconducting Condensate in Cuprate Superconductors by Femtosecond Photoexcitation. *Phys. Rev. Lett.* **101**, 227001 (2008).
58. Mertelj, T. *et al.* Distinct Pseudogap and Quasiparticle Relaxation Dynamics in the Superconducting State of Nearly Optimally Doped  $\text{SmFeAsO}_{0.8}\text{F}_{0.2}$  Single Crystals. *Phys. Rev. Lett.* **102**, 117002 (2009).
59. Owen, C.S., & Scalapino, D.J. Superconducting State under the Influence of External Dynamic Pair Breaking. *Phys. Rev. Lett.* **28**, 1559 (1972).
60. Rothwarf, A. & Taylor, B. N. Measurement of Recombination Lifetimes in Superconductors. *Phys. Rev. Lett.* **19**, 27 (1967).
61. Gay, P. *et al.*, Femtosecond Dynamics of BSCCO-2212. *J. Low Temp. Phys.* **117**, 1025 (1999).
62. Smith, D. *et al.*, Femtosecond dynamics of BSCCO-2212 in the weak and strong excitation limits. *Physica C* **341**, 2221 (2000).
63. Dvorsek, D. *et al.* Femtosecond quasiparticle relaxation dynamics and probe polarization anisotropy in  $\text{YSr}_x\text{Ba}_{2-x}\text{Cu}_4\text{O}_8$ . *Phys. Rev. B* **66**, 0205100 (2002).